Journal of Thermal Analysis, Vol. 42 (1994) 647-665

DIFFERENTIAL SCANNING CALORIMETRY AND THE ADVANCED SOLIDIFICATION PROCESSING OF METALS AND ALLOYS

B. Cantor

Oxford Centre for Advanced Materials and Composites, Department of Materials, Oxford University, Parks Rd, Oxford OX1 3PH, UK

Abstract

This paper describes some examples of the use of differential scanning calorimetry (DSC) in providing information for advanced solidification processing of metals and alloys. Spray forming, squeeze casting, grain refinement and crystallization of amorphous alloys are all discussed. DSC measurements are shown to be valuable for testing kinetic theories of nucleation and growth, and validating solidification process models.

Keywords: alloys, crystallization, DSC, solidification, processing

Introduction

A wide range of advanced solidification processing methods have been developed to manufacture novel metallurgical materials for industrial applications. In general, sophisticated levels of process control are needed to maintain operations within a tight window of thermal and mass flow conditions, and thus ensure that the final material microstructures and properties remain within specification [1]. Unfortunately, our understanding of the kinetics of nucleation and growth during solidification is not good enough to predict the behaviour of industrial allow systems in complex processing environments [2]. Optimizing operating conditions is usually achieved, therefore, by inconvenient and uncertain trial and error testing under plant conditions.

Calorimetric techniques are particularly convenient for monitoring the kinetics of phase transformations such as solidification. Changes in heat content in a solidifying material are directly proportional to the amount of solidification which has taken place, and are closely related to the thermodynamic forces driving the solidification process. Calorimetric data can be used to test kinetic theories of nucleation and growth during solidification, and to validate models of solidification processes for on- and off-line control [1, 3].

0368–4466/94/ $ 4.00

John Wiley & Sons, Limited
Chichester

The objective of this paper is to describe some examples of the use of differential scanning calorimetry (DSC) in providing information for advanced solidification processing of metals and alloys. The following processes are discussed: spray forming of Al alloy and Al alloy/SiC particulate composite extrusion and forging billets for high specific strength and stiffness aerospace structural components; squeeze casting of Al–Si alloys and Al alloy/Al_2O_3 discontinuous fibre composites for high integrity wear-resistant automotive components; grain refinement by addition of nucleating agents to improve the homogeneity of ingots and castings; melt spinning of amorphous Fe–Si–B soft ferromagnetic alloys for low loss distribution transformer cores; and crystallization of amorphous Fe-transition metal-B alloys as in-situ Fe/boride particulate composites for high specific strength and stiffness areoengine components.

Solid fraction *vs.* temperature

DSC measurements

Modelling and control of advanced solidification processes requires accurate data for the evolution of solid fraction and latent heat during cooling [1, 3]. Unfortunately, the progress of solidification cannot be predicted quantitatively for multicomponent industrial alloys under complex thermal conditions during processing. However, DSC methods have now been developed to measure solid fraction and latent heat release directly [4, 5].

The DSC measurements are quite straightforward, involving heating an alloy above its liquidus temperature, and then re-cooling to monitor the heat output during solidification. Integrating the resulting DSC trace gives directly the temperature variation of solid fraction at the imposed cooling rate in the DSC. The main experimental problems are as follows [4, 5].

(1) Nucleation of solidification is often suppressed to below the liquidus temperature, unlike nucleation in industrial processes which is usually stimulated by impurities or nucleating agents.

(2) Solute partitioning extends solidification to below the solidus temperature, so that latent heat is emitted over a broad temperature range, making it difficult to construct a suitable baseline for integration.

(3) Latent heat evolution can be obscured by heat given out by reactions between the liquid alloy and the DSC specimen container.

(4) DSC cooling rates are typically 1–40 deg·min^{-1}, quite often but not always comparable to industrial processing conditions.

Graphite and tungsten-lined copper specimen containers are found to give acceptable results for the melting and solidification of a wide range of commer-

cial Al alloys, as long as the specimen is maintained in the liquid state for as short a time as possible [4, 5]. DSC has been used to generate solid fraction *vs.* temperature results for a range of model and industrial Al alloys, as listed in Table 1. Figure 1 shows a typical DSC trace and the corresponding variation of solid fraction with temperature for the high strength, temperature resistant, wrought Al alloy 2618 (Al-2.5 wt%Cu-1.5 wt%Mg-1 wt%Fe-1 wt%Mn). In-

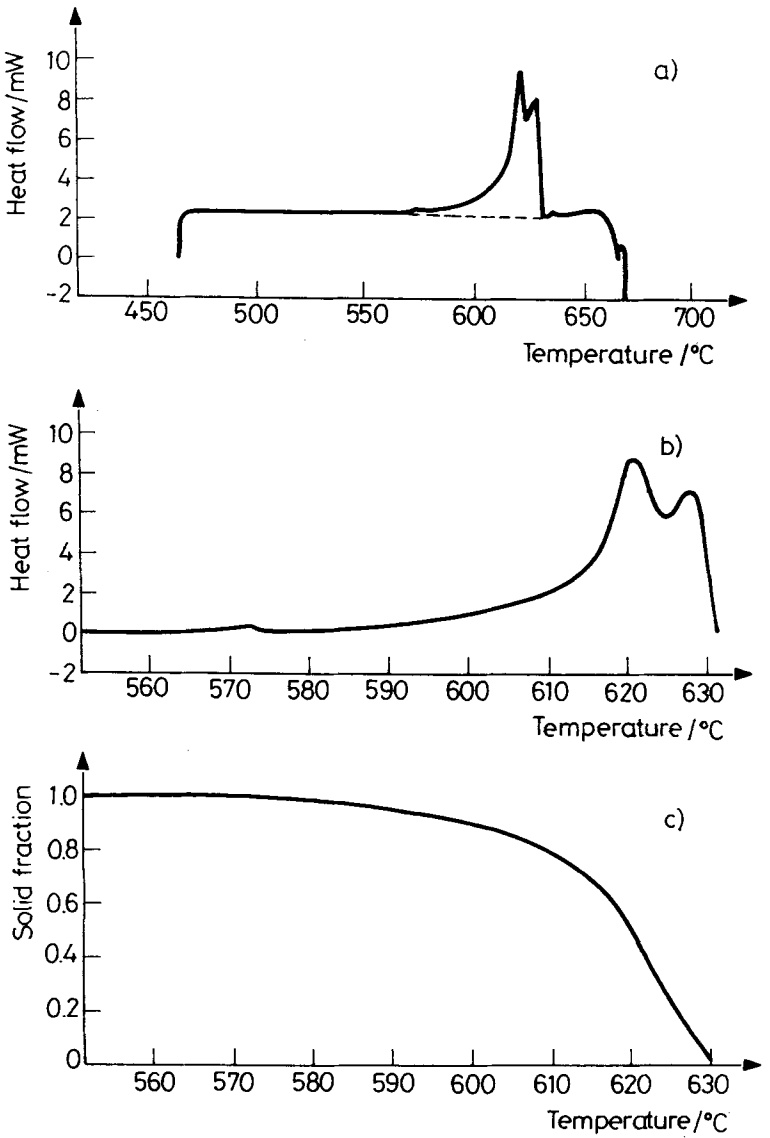

Fig. 1 (a) DSC trace, (b) solidification exotherm and (c) integrated solid fraction for 2618

tegrating a DSC trace gives the total latent heat of solidification, and measured values are listed in Table 1. The next two sections describe applications of DSC results such as shown in Fig. 1 to the modelling of advanced solidification processes.

Table 1 Al alloys used to measure fraction solid *vs.* temperature by DSC, together with integrated latent heats

Alloy	Type	Latent heat / $kJ \cdot kg^{-1}$
2014	Al–Cu–Mg	288
2024	Al–Cu–Mg	325
2124	Al–Cu–Mg	310
2618	Al–Cu–Mg	290
997	Al	385
6061	Al–Mg–Si	329
6063	Al–Mg–Si	371
7075	Al–Cu–Mg–Zn	367
7150	Al–Cu–Mg–Zn	345
7475	Al–Cu–Mg–Zn	362
8090	Al–Cu–Mg–Li	388
8091	Al–Cu–Mg–Li	326
LM13	Al–Si–Mg	450

Spray forming

The development and improvement of aerospace structures places a premium on light materials with high stiffness and strength [6, 7]. Spray formed Al alloy and composite extrusion and forging billets are being manufactured for these applications [8–10]. Figure 2 shows a schematic diagram of the spray forming process [3, 8]. An alloy is melted, superheated 100–300°C above its melting point, and then bottom poured through a 1–5 mm diameter nozzle into the top of the spray forming chamber. The melt stream is atomized by the impingement of 100–300 m/s gas jets to create a spray of 5–500 μm sized alloy droplets, which deposits on a collector plate interspersed in the spray plume. Collector and deposit are reciprocated or rotated and withdrawn synchronously with the metal feed to build up a cylindrical or flat slab billet. Composites are manufactured by entraining SiC particulate in the spray plume to co-deposit on the collector plate [1, 8].

Minimizing as-spray formed porosity, matrix grain size and second phase aluminide particle size is essential to guarantee material integrity and increase ductility and fracture toughness [8–10]. This requires careful control of the

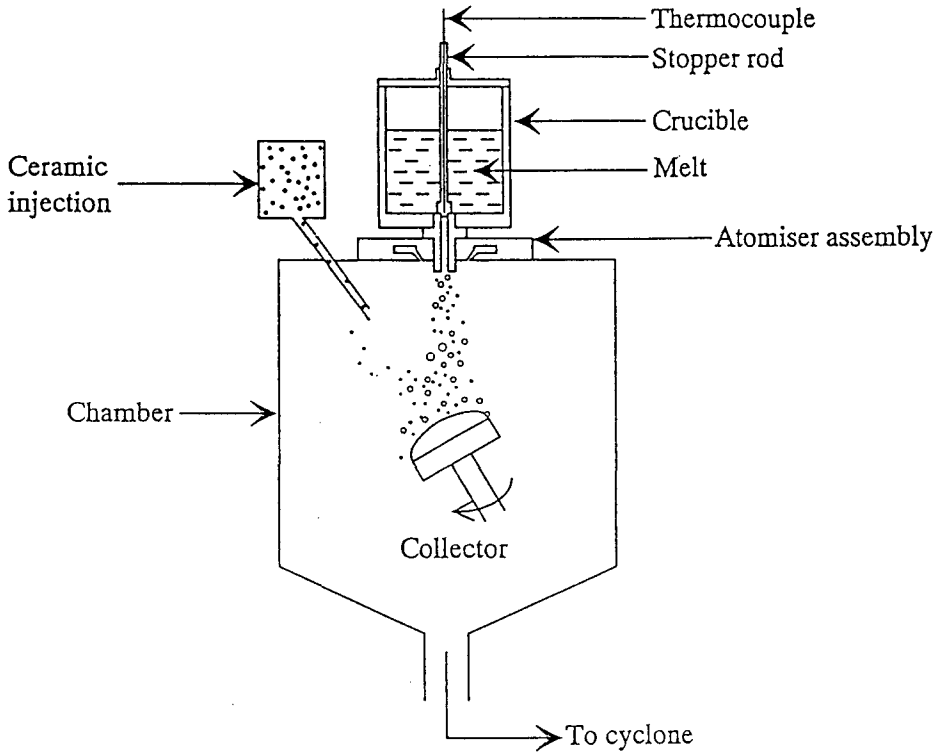

Fig. 2 Schematic diagram of spray forming

molten alloy cooling behaviour. Alloy superheat and latent heat are removed partially from the droplets during flight, and partially from the top surface of the billet after the droplets and SiC have deposited [8]. The gas, melt and SiC flow rates must be manipulated to ensure that the arriving spray and the billet top surface are both in a semi-solid state. Too liquid a spray leads to splashing, incorporated gas porosity, grain growth and coarse aluminides; too solid a spray leads to incorporation of pre-solidified droplets, shrinkage porosity and inhomogeneous splat structures.

Figure 3 shows computer calculated variations in droplet velocity v, temperature T and solid fraction f with flight distance during spray forming of Al alloy 7075 (Al-5.6 wt%Zn-2.5 wt%Mg-1.6 wt%Cu-0.23 wt%Cr) with an inlet gas velocity of 150 m/s and a melt superheat of 150°C [3]. The droplet velocities were calculated from Newton's second law of motion [11–13], using laser Doppler anemometer (LDA) measurements of gas velocity V_g:

$$m\mathrm{d}v/\mathrm{d}t = c\pi r^2\rho(v_g - v)^2 \quad (1)$$

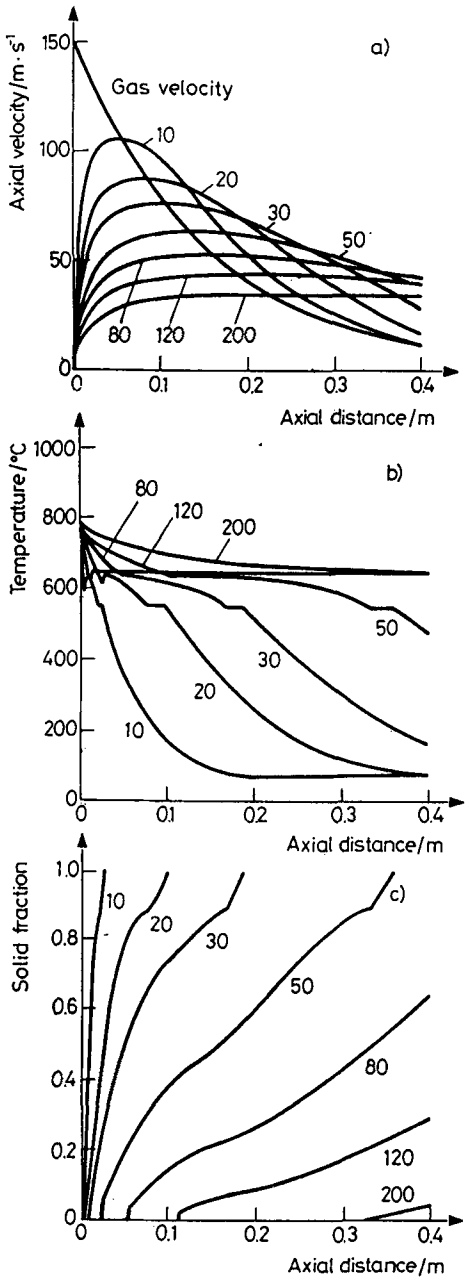

Fig. 3 Computer calculations of (a) droplet velocity, (b) temperature and (c) solid fraction during spray forming of 7075

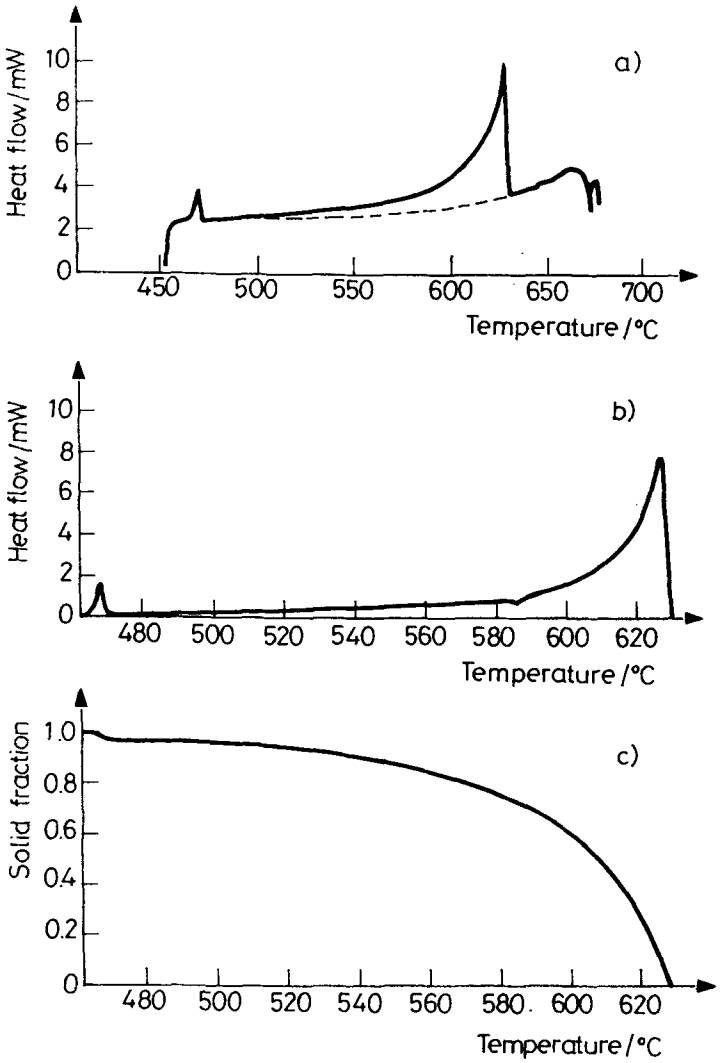

Fig. 4 (a) DSC trace, (b) solidification exotherm and (c) integrated solid fraction for 7075

where m, r and ρ are the droplet mass, radius and density respectively, and c is the drag coefficient. The droplets accelerate and then decelerate with velocities which are very sensitive to droplet size. The droplet temperatures and solid fractions were calculated from Newton's law of cooling [11–13], using DSC measurements of solid fraction as shown in Fig. 4:

$$-3h(T - T_g) = \rho r(C\mathrm{d}T/\mathrm{d}t - L\mathrm{d}f/\mathrm{d}t) \quad (2)$$

where C and L are the droplet specific and latent heat respectively, h is the heat transfer coefficient and T_g is the gas temperature. Droplet cooling and solidification behaviour are again very sensitive to droplet size. Figure 5 shows computer calculated variations of the top surface temperature of a 7075 spray formed billet at 0.31 m from the atomizer, obtained from a 1-D billet heat flow model after integrating the individual droplet results in Fig. 3 over a sieve-measured droplet size distribution, and again using the DSC measurements of solid fraction in Fig. 4 [3]. Infra-red thermal imaging measurements agree reasonably well with the calculated top surface temperatures [3, 13], as shown in Fig. 5.

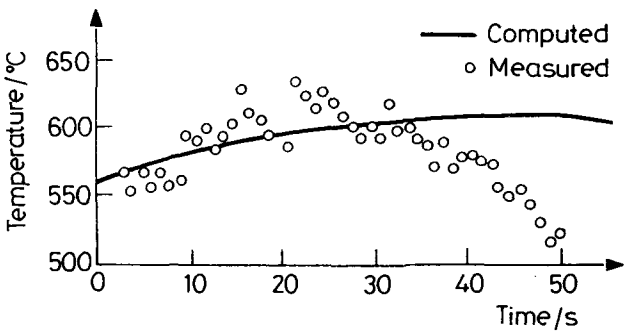

Fig. 5 Computer calculations of top surface temperature and corresponding infra-red measurements during spray forming of 7075

Squeeze casting

Environmental issues such as energy consumption, recycling and pollution are causing rapid improvements in automotive fuel efficiency. Without impairing roadholding and comfort, this requires a reduction in the dynamic loads transmitted from the vehicle frame to the suspension system, which in turn requires a reduction in the unsprung mass. Thus, squeeze cast Al alloys and composites are being manufactured to replace cast iron and steel automotive components [14–16]. Figure 6 shows a schematic diagram of the squeeze casting process [14, 15]. An alloy is melted, superheated 100–300°C above its melting point, injected into a preheated die cavity at 300–500°C, and then pressurized up to 1–200 MPa during cooling and solidification. Composites are manufactured by infiltrating a fibre preform inserted in the die [1, 14].

Minimizing porosity, solute segregation and grain size is essential to enhance as-cast mechanical properties and compete with cast iron and steel in high volume, low cost automotive markets [14–16]. This again requires careful control of the molten alloy cooling behaviour. Alloy superheat and latent heat are removed rapidly from the melt by the die, and it is difficult to prevent partial

solidification before reaching full pressure [15, 16]. The melt, die and ram temperatures and the ram travel must be manipulated to ensure that die filling is followed smoothly and rapidly by pressurization. Too rapid pressurization leads to poor filling and low tolerances; too slow pressurization leads to alloy segregation and poor infiltration.

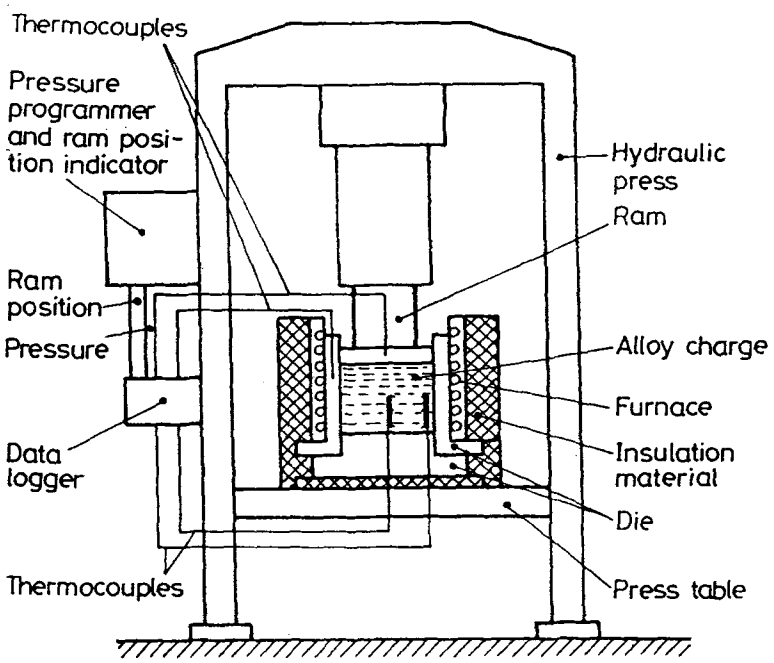

Fig. 6 Schematic diagram of squeeze casting

Figure 7 shows computer calculated variations of temperature with time at the ingot centre and die inner surface during squeeze casting of the automotive Al casting alloy A356 (Al-7 wt%Si-0.3 wt%Mg) into a 50 mm diameter, 80 mm long, cylindrical H13 tool steel die cavity, with low applied pressure corresponding to an ingot/die heat transfer coefficient of 2 kW/m^2K and initial melt and die temperatures of 750 and 300°C respectively [16]. The calculations used finite difference methods in cylindrical coordinates to solve the thermal diffusion equation for the solidifying ingot material, using DSC measurements of solid fraction similar to Figs 1 and 4:

$$C\mathrm{d}T/\mathrm{d}t + L\mathrm{d}f/\mathrm{d}t = (k/\rho)\nabla^2 T \qquad (3)$$

where k is the thermal conductivity. Heat flow in the squeeze casting die and ram were included by ignoring the second term, and the boundary conditions were Newtonian:

$$C\mathrm{d}T/\mathrm{d}t = (k/\rho)\nabla T - h\Delta T \tag{4}$$

where ΔT is the temperature difference across the boundary, and different time variations of heat transfer coefficient h were used at the boundaries between ingot, die, ram and surrounding atmosphere. The die temperature rises and the ingot cools and solidifies rapidly, as alloy superheat and latent heat are extracted from the melt. Embedded thermocouple measurements of alloy cooling behaviour agree well with the calculated temperatures, as shown in Fig. 7 [16].

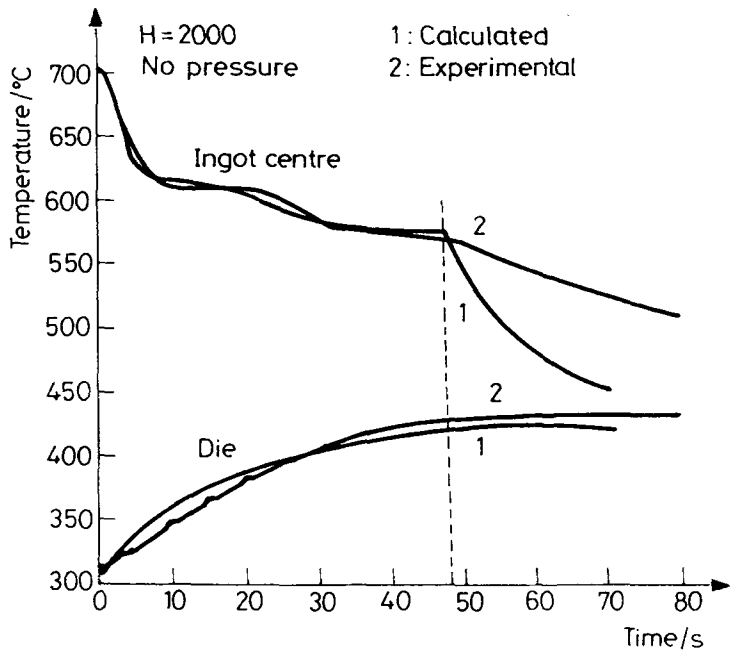

Fig. 7 Computer calculations and embedded thermocouple measurements of ingot and die temperatures during squeeze casting of A356

Heterogeneous nucleation and grain refinement

DSC measurements

The nucleation pattern during solidification processing determines many important microstructural features, such as grain size and shape, phase structure and extent of solute segregation, all of which exert a strong influence on the fi-

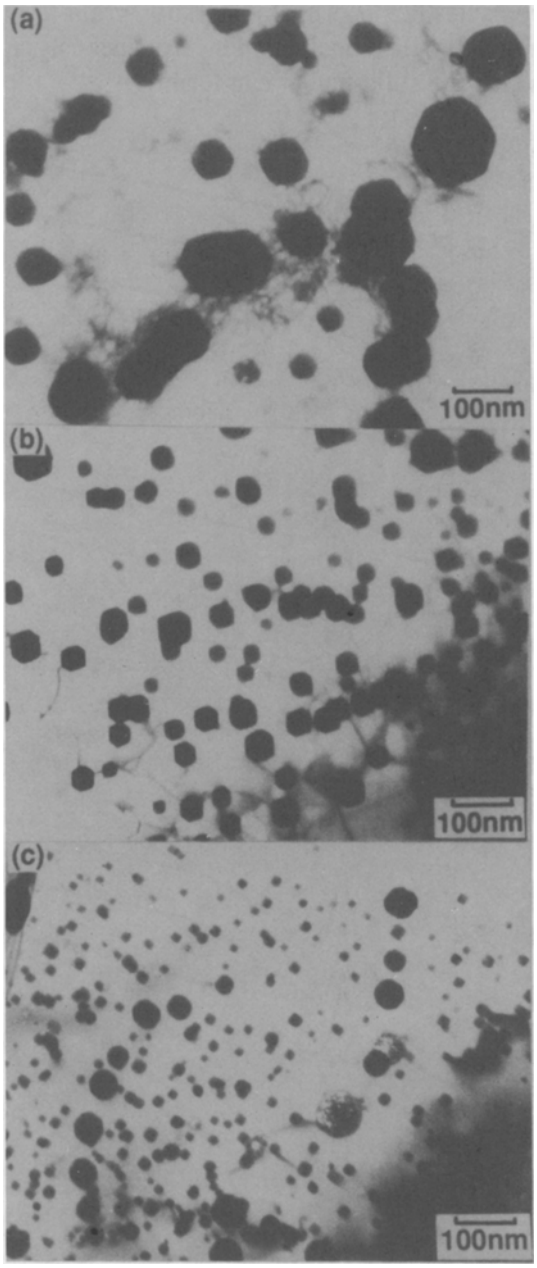

Fig. 8 Transmission electron micrographs of Al-7 wt%In melt spun at (a) 7 m/s, (b) 14 m/s and (c) 65 m/s

nal mechanical properties [2, 17, 18]. Industrially, grain refining agents such as Al–Ti–B are added to stimulate nucleation heterogeneously, i.e. to provide catalyst surfaces on which the solid nuclei can form [19].

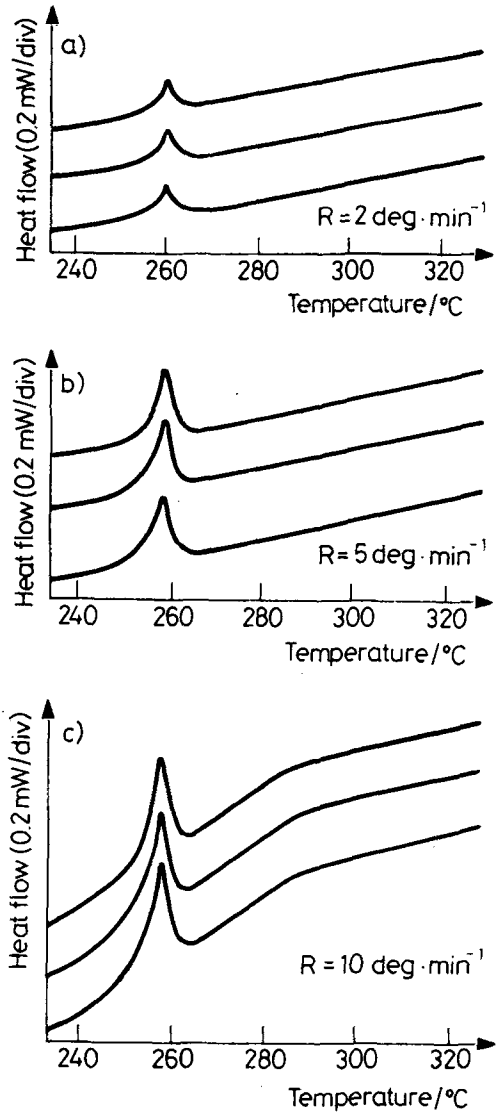

Fig. 9 DSC traces of Cd droplet solidification exotherms in Al-4.5 wt% Cd

Controlled and reproducible experimental techniques for investigating the heterogeneous nucleation of solidification are difficult to achieve, because the nucleation process is highly sensitive to catalytic trace impurities [2, 18]. A

DSC method has been developed to overcome this problem [20–24]. An alloy consisting of 10–100 nm sized liquid droplets embedded in a solid matrix is cooled below the melting point, and droplet solidification is nucleated heterogeneously by the surrounding matrix. The kinetics of nucleation are monitored by DSC, and the solidified microstructures are monitored by transmission electron microscopy. By dividing the liquid into a large number of small droplets, trace impurities are segregated into relatively few droplets and thus rendered harmless [20–24].

Figure 8 shows typical microstructures in a melt spun Al-7 wt%In alloy, consisting of 10^{19}–$10^{20}/m^3$, 10–100 nm sized In particles in an Al matrix [25]. Figure 9 shows typical DSC traces of Cd droplet solidification exotherms in an Al-4.5 wt%Cd alloy. The Cd droplets are heterogeneously nucleated on {111} facets of the surrounding Al matrix, with an onset temperature corresponding to an undercooling of 56 K below the Cd melting point [24]. Similar results have been obtained for a range of alloy systems as shown in Table 2, with measured undercooling often reproducible to better than ±0.5 K.

Table 2 Heterogeneous nucleation temperatures, contact angles and site densities obtained from embedded droplet DSC experiments

Alloy	ΔT/ K	θ /°	N_c /particle
Cu–Pb	0.5	4	10^{-12}
Al–Pb	22	21	10^{-6}
Zn–Pb	30	23	10^{-8}
Al–In	13	27	10^{-7}
Al–Cd	56	42	30
Al–Sn	104	59	100

Nucleation mechanism

The classical model of heterogeneous nucleation assumes that solid nuclei form as spherical caps on the catalyst/liquid interface, as shown in Fig. 10. The fraction of solidified droplets Z depends upon the nucleation rate J [18, 26, 27].

$$dZ/dt = J(1-Z) \tag{5}$$

$$J = aN_c \exp(-bg/\Delta T^2 T) \tag{6}$$

where a and b are material constants, N_c is the density of available nucleation sites on the catalyst surface, $g = 1/4(2-3\cos\theta+\cos^3\theta)$ is the catalytic efficiency, θ is the contact angle at the catalyst/solid/liquid triple point as shown in Fig. 10, and $\Delta T = T_m - T$ is the undercooling below the melting point T_m.

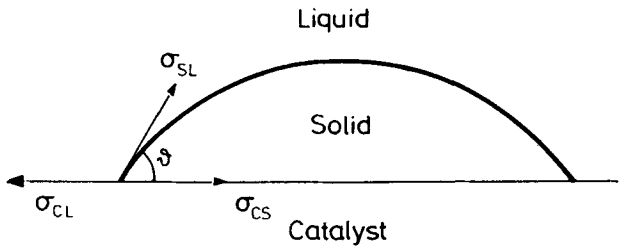

Fig. 10 Schematic diagram of the spherical cap model of heterogeneous nucleation

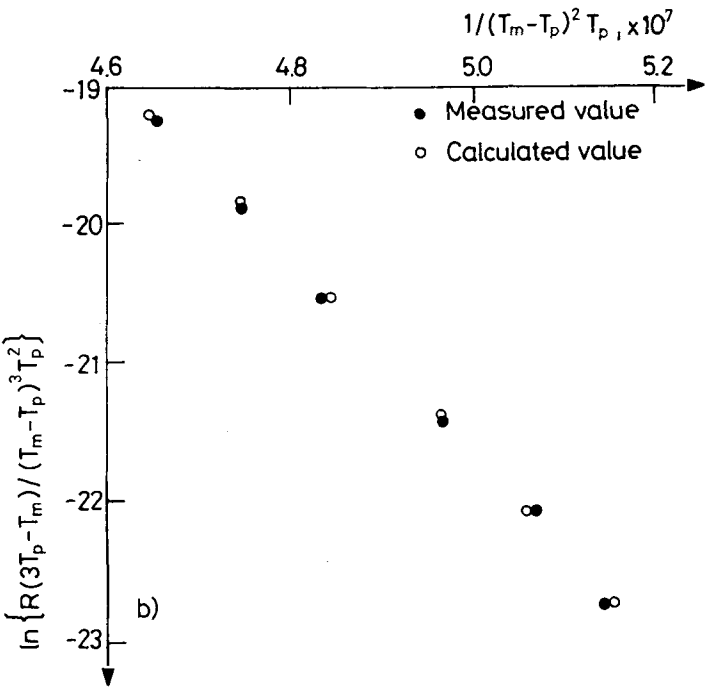

Fig. 11 $\mathrm{Ln}\{R(3T_p-T_m)/(T_m-T_p)^3T_p^2\}$ *vs.* $1/(T_m-T_p)^2T$ measured from the Cd droplet solidification exotherms in Fig. 9 and calculated from Eq. (7)

Differentiating Eqs (5) and (6) gives the variation of peak temperature T_p with cooling rate R for DSC traces such as shown in Fig. 9 [27]:

$$bgR\,(3T_p - T_m) / aN_c(T_m - T_p)^3T_p^2 = \exp -bg / (T_m - T_p)^2T_p \qquad (7)$$

Equation (7) predicts a linear variation of $\ln\{R(3T_p-T_m)/(T_m-T_p)^3T_p^2\}$ with $1/(T_m-T_p)^2T$, with a slope and intercept determined by θ and N_c. Figure 11 shows typical results for the Cd solidification exotherms in Fig. 9 [24, 27].

Measured values of θ and N_c are included in Table 2. Poor catalysts with high θ show reasonable agreement with the classical theory of Eqs (5)–(7), but good catalysts with low θ give unphysical values of N_c [28, 29]. The classical theory fails because the spherical cap in Fig. 10 becomes unreasonable thin when θ is less than ~20°.

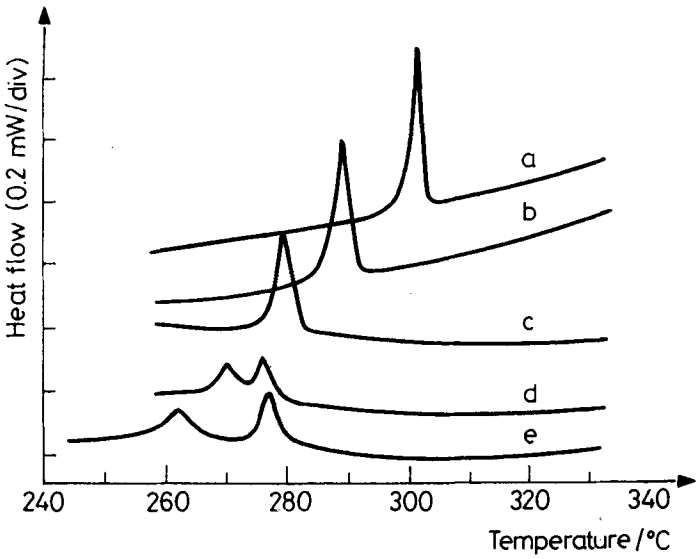

Fig. 12 DSC traces of Pb droplet solidification exotherms in Al-5 wt%Pb doped with (a) 0 wt%Ge, (b) 0.5 wt%Ge, (c) 1 wt%Ge, (d) 1.5 wt%Ge and (e) 2 wt%Ge

Doping experiments can be used to investigate the effect of impurities on heterogeneous nucleation. Figure 12 shows typical DSC results for the effect of Ge on heterogeneous nucleation of Pb droplets by the surrounding Al matrix. Al dissolves up to 1 wt%Ge, and its catalytic efficiency deteriorates, i.e. Pb solidification is nucleated at larger undercooling [30]. Similar experiments show that P enhances the catalytic efficiency of Al as a nucleant for Si solidification [31, 32].

Crystallization of amorphous alloys

DSC measurements

Amorphous alloys crystallize by a variety of complex reactions [33]. Understanding and controlling the crystallization of amorphous alloys is necessary in some cases to manufacture a devitrified product, and in other cases to prevent unwanted devitrification in service. For example, melt spun amorphous FeSiB

alloys exhibit low magnetic hysteresis losses and are attractive as transformer cores, but must be prevented from crystallizing under working conditions [34–40]. As another example, melt spun or atomized amorphous FeCrXB alloys, where X is a transition metal, can be crystallized during heat treatment and consolidation to produce materials with high specific strength and stiffness for structural applications, but the crystallized microstructure must be carefully manipulated to ensure appropriate mechanical properties [41–44].

Figures 13 and 14 show typical DSC traces for the crystallization of amorphous $Fe_{78}Si_9B_{13}$ and $Fe_{65}Cr_{18}Ti_2B_{15}$ respectively during continuous heating at 5–80 deg·min^{-1} and isothermal annealing at 495–520°C [38, 39]. The crystal-

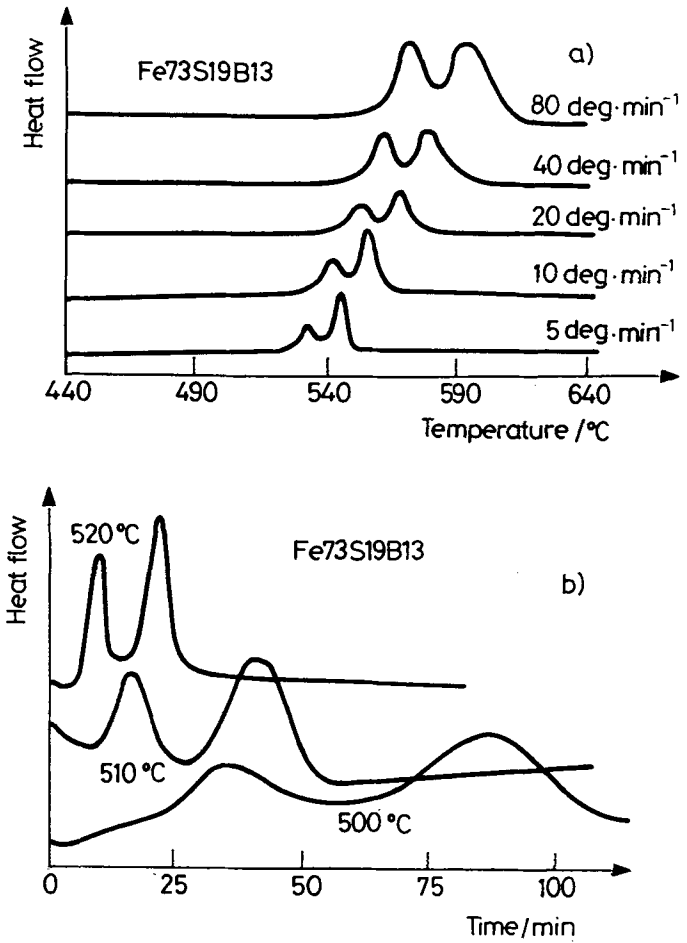

Fig. 13 DSC traces of the crystallization of amorphous $Fe_{78}Si_9B_{13}$ during (a) continuous heating and (b) isothermal annealing

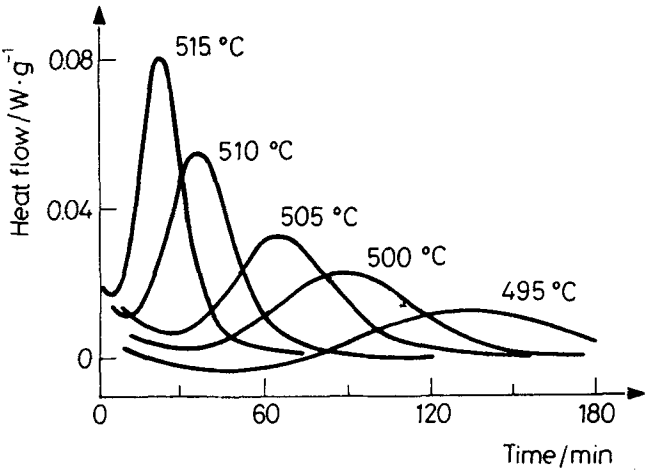

Fig. 14 DSC traces of the crystallization of amorphous $Fe_{65}Cr_{18}Ti_2B_{15}$ during isothermal annealing

lization temperatures increase with increasing heating rate, and the crystallization kinetics increase with increasing annealing temperature.

Crystallization mechanism

Tables 3 and 4 summarise the phases found in crystallized $Fe_{78}Si_9B_{13}$ and $Fe_{70}Cr_{18}Mo_2B_{10}$ respectively by X-ray diffractometry and transmission electron microscopy after annealing at different temperatures [38, 39, 45–48]. The crystallized microstructures consist of fine-scale multiphase mixtures, with the prevalence of different phases depending sensitively on annealing temperature.

Table 3 Phases in crystallized $Fe_{78}Si_9B_{13}$ after annealing at different temperatures

T/°C	Matrix	Other phases
450	bcc ferrite	none
510	bcc ferrite	tetragonal M_3B+eutectic ferrite /M_3B
600	bcc ferrite	DO_3Fe_3Si+orthorhombic M_2B

Amorphous alloy crystallization kinetics often obey the Johnson-Mehl-Avrami equation [17, 45].

$$f = 1 - \exp\{-(Kt)^n\} \tag{8}$$

where f is the crystalline fraction after an annealing time t, obtained by integrating DSC traces such as shown in Figs 13 and 14, n is the Avrami exponent, and

K is the crystallization rate constant. For $Fe_{78}Si_9B_{13}$, the measured Avrami exponent is $n = 4$, corresponding to bulk nucleation and linear 3-D growth of polymorphic or eutectic crystals [38, 39, 45]. Microstructural measurements of crystal number densities and sizes also show linear nucleation and growth kinetics. For $Fe_{70}Cr_{18}Mo_2B_{10}$, the measured Avrami exponent is $n = 3$, corresponding to linear 3-D growth of polymorphic or eutectic crystals on pre-existing nuclei [46–48]. The apparent simplicity of the crystallization kinetics is surprising, given the microstructural complexity shown in Tables 3 and 4, making it unwise to predict crystallization behaviour by extrapolation to lower temperatures.

Table 4 Phases in crystallized $Fe_{70}Cr_{18}Mo_2B_{10}$ after annealing at different temperatures

T/°C	Matrix	Borides
500 and 600	bcc ferrite	Cr rich bct M_3B
700 and 800	bcc ferrite	Cr rich orthorhombic M_2B + Mo rich fcc $M_{23}B_6$
900	bct martensite	Cr rich orthorhombic M_2B + Mo rich fcc $M_{23}B_6$
950 and 1000	bct martensite	Cr rich orthorhombic M_2B + Mo rich tetragonal M_3B_2

Conclusions

DSC measurements can be used to obtain information about the kinetics of nucleation and growth during the solidification and crystallization of metals and alloys. DSC measurements can be used to test kinetic theories and solidification process models.

References

1 B. Cantor, J. Microscopy, 169 (1993) 97.
2 W. Kurz and D. J. Fisher, 'Fundamentals of Solidification', Trans. Tech., Switzerland, 1989.
3 P. S. Grant and B. Cantor, Cast Metals, 4 (1991) 140.
4 A. P. Newbery, Part II thesis, Oxford University, 1988.
5 P. S. Grant, D. L. Zhang, L. Katgerman and B. Cantor.
6 'Metal Matrix Composites: Technology and Industrial Applications' Techtrends, Innovation, Paris 1990, p. 128.
7 E. A. Feest, Metals and Materials, 4 (1988) 273.
8 T. C. Willis, Metals and Materials, 4 (1988) 485.
9 R. G. Brooks and J. V. Wood, 'ICSF-1' Osprey Metals, Swansea, 1991.
10 R. G. Brooks and J. V. Wood, 'ICSF-2' Osprey Metals, Swansea, 1993.
11 P. S. Grant, B. Cantor and L. Katgerman, Acta Metals Mater., 41 (1993) 3097.
12 P. S. Grant, B. Cantor and L. Katgerman, Acta Metals Mater., 41 (1993) 3109.
13 P. S. GrantP. P. Maher and B. Cantor, Mater. Sci. Eng., A179/A180 (1994) 72.
14 M. Jolly, The Foundryman, (1990) 509.
15 D. L. Zhang, C. Brindley and B. Cantor, J. Mater. Sci., 28 (1993) 2267.

16 D. L. Zhang and B. Cantor, 'Modelling of squeeze casting': submitted to Modelling Simulation in Materials Science Engineering.
17 J. W. Christian, 'The Theory of Transformations in Metals and Alloys', Pergamon, Oxford 1975.
18 D. Turnbull, J. Appl. Phys., 21 (1950) 1022.
19 W. T. Kim, B. Cantor, W. D. Griffth and M. R. Jolly, Int. J. Rapid. Solidification, 7 (1992) 245.
20 C. C. Wang and C. S. Smith, Trans. Metals Soc, AIME, 188 (1950) 136.
21 R. T. Southin and G. A Chadwick, Acta Metall, 26 (1978) 223.
22 P. G. Boswell and G. A. Chadwick, Acta Metall, 28 (1980) 209.
23 K. I. Moore, D. L. Zhang and B. Cantor, Acta Metall Mater, 38 (1990) 1327.
24 D. L. Zhang, K. Chattopadhyay and B. Cantor, J. Mater Sci., 26 (1991) 1531.
25 D. L. Zhang and B. Cantor, Philos Mag., 62 (1990) 557.
26 B. Cantor and R. D. Doherty, Acta Metals, 27 (1979) 33.
27 W. T. Kim, D. L. Zhang and B. Cantor, Metall. Trans., 22A (1991) 2478.
28 W. T. Kim and B. Cantor, Acta Metall. Mater., 40 (1992) 3339.
29 K. A. Q. O'Reilly and B. Cantor, Acta Metal. Mater., in press.
30 D. L. Zhang and B. Cantor, J. Cryst. Growth, 104 (1990) 583.
31 C. R. Ho and B. Cantor, Mater. Sci. Eng. A173 (1993) 37.
32 D. L. Zhang and B. Cantor, Metals. Trans., 24A (1993) 1195.
33 S. Savage and H. Fredriksson (eds) 'Rapidly Quenched Materials 7', Elsevier, Amsterdam 1991.
34 V. R. V. Ramaman and G. E. Fish, J. Appl. Phys., 53 (1982) 2273.
35 A. Zaluska and H. Matyja, J. Mater. Sci., 18 (1983) 2163.
36 M. A. Gibson and G. W. Delamore, J. Mater. Sci., 22 (1987) 4550.
37 C. F. Chang and J. Marti, J. Mater. Sci., 18 (1983) 2297.
38 M. A. Hughes, A. R. Bhatti, W. Gao and B. Cantor, Materials Forum (Australi Bicentenary Volume) 11 (1988) 21.
39 M. A. Hughes, K. Ishii, W. T. Kim, A. R. Bhatti and B. Cantor, 'Amorphous Metallic Materials 3' eds P. Duhaj, P. Mrafko and P. Svec, Trans. Tech., Switzerland, 1992, p. 25.
40 R. Ray, 'Rapidly Solidified Amorphous and Crystalline Alloys' eds B. H. Kear, B. C. Giessen and M. Cohen, North Holland, New York 1982, p. 435.
41 M. J. Rawson et al., in 'Rapidly Solidified Materials: Properties and Processing' eds P. W. Lee and J. H. Mole, ASM, Metals Park 1988, p. 37.
42 S. Hahn, S. Isserow and R. Ray, J. Mater. Sci., 22 (1987) 3395.
43 R. Ray, V. Panchanathan and S. Isserow, J. Metals, 35 (1983) 30.
44 S. Hahn, S. Isserow and R. Ray, J. Mater. Sci. Lett., 4 (1985) 972.
45 W. Gao and B. Cantor, Acta Metall, 36 (1988) 2293.
46 W. T. Kim, B. Cantor, K. Clay and C. Small, 'Fundamental Realationships Between Microstructure and Mechanical of Metal Matrix Composites' eds P. K. Liaw and M. N. Gungor, AIME, Warrendale, 1990, p. 89.
47 W. T. Kim, K. Clay, C., Small and B. Cantor, J. Non-Cryst. Solids, 127 (1991) 273.
48 I. T. H. Chang, K. Ishii and B. Cantor, Mater. Sci. Eng. A179/A180 (1994) 416.

Zusammenfassung — Vorliegend werden einige Beispiele für den Einsatz von DSC zur Gewinnung von Informationen über Erstarrungsprozesse von Metallen und Legierungen beschrieben. Dabei wurden sowohl Spritzformen, als auch Druckgießen, Kornverfeinerung und Kristallisation von amorphen Legierungen behandelt. DSC-Messungen erweisen sich als nützlich für das Testen der kinetischen Theorien von Keimbildung und Keimwachstum und zur Bestätigung der Erstarrungsprozeßmodelle.